Environmental
Science
Water Research & Technology

ROYAL SOCIETY
OF CHEMISTRY

PAPER

View Article Online
View Journal | View Issue

Check for updates

Cite this: *Environ. Sci.: Water Res. Technol.*, 2024, **10**, 2087

# Efficient visible-light-driven photocatalysis: simultaneous degradation of multiple pollutants with bismuth oxyhalide solid solutions†

Helena Pérez del Pulgar, [a] Josefa Ortiz-Bustos, [a] Santiago Gómez-Ruiz, [ab] Isabel del Hierro *[ab] and Yolanda Pérez *[ac]

Received 24th May 2024,
Accepted 22nd June 2024

DOI: 10.1039/d4ew00410h

rsc.li/es-water

Visible-light-driven photocatalysis is considered as a sustainable and cost-effective method for water remediation. In aquatic environments, the coexistence of multiple contaminants, such as organic and inorganic compounds, poses a potential threat to both biological organisms and human health, complicating their removal. Despite the urgent need for the development of comprehensive solutions, the research on the concurrent and simultaneous removal of multiple pollutants remains limited primarily relies on photocatalysts based on heterojunctions. To address this issue, we have prepared $BiOCl_{0.9}I_{0.1}$ and $BiOBr_{0.9}I_{0.1}$ solid solutions, exhibiting well-tailored band gaps and energetics of the conduction and valence bands, using an easy chemical precipitation approach. These synthesized materials exhibited exceptional photocatalytic efficacy under visible light, effectively removing a complex mixture of contaminants, including ciprofloxacin (CIP), methylparaben (MP), and rhodamine B (RhB), from water. Particularly noteworthy was the outstanding performance of $BiOCl_{0.9}I_{0.1}$, which demonstrated a complete removal of RhB within 10 min, CIP within 40 min, and an 86% degradation of MP within 40 min. This superior performance can be attributed to the materials' exceptional optical and (photo)electrochemical properties. Furthermore, the synergistic or antagonistic effects coexisting contaminants, organic matter, and inorganic ions on the photodegradation process were also investigated. Additionally, the generation of reactive oxygen species (ROS), and the elucidation of the degradation pathways were examined providing valuable insights into the intricate interplay of environmental factors that may have an influence on the photocatalytic performance. Our study shows, therefore, the high potential of $BiOCl_{0.9}I_{0.1}$ and $BiOBr_{0.9}I_{0.1}$ as promising candidates for the simultaneous removal of diverse water pollutants, offering a robust and efficient approach towards advancing water purification technologies.

### Water impact

Visible-light active $BiOCl_{0.9}I_{0.1}$ and $BiOBr_{0.9}I_{0.1}$ materials have demonstrated to be robust and efficient photocatalysts for the concurrent and simultaneous removal of contaminants (*i.e.* methylparaben, ciprofloxacin and rhodamine B). We have examined the synergistic or antagonistic effects of coexisting contaminants, organic matter, and inorganic ions on the photodegradation process towards more realistic water conditions.

## 1. Introduction

Water pollution is a mayor global concern that affects not only aquatic ecosystems, but also humans and animals. Recalcitrant contaminants[1] including pharmaceutical and personal care products (PPCPs), pesticides, flame retardants, and organic dyes, predominantly enter the environment through effluents from wastewater treatment plants, as conventional decontamination methods prove ineffective in their removal. For instance, the antibiotic ciprofloxacin, which is linked to antibiotic resistance, has been detected in hospital effluents from Spain, Sweden, Portugal, and Italy at high concentrations (μg $L^{-1}$),[2] as well as in drinking and surface water.[3] Parabens, associated with possible endocrine-disrupting effects,[4] are mainly found in surface water at high concentrations (170.9 μg $L^{-1}$ and 52.1 μg $L^{-1}$ for methylparaben (MeP) and propylparaben (ProP),

---

[a] *COMET-NANO Group, Departamento de Biología y Geología, Física y Química Inorgánica, ESCET, Universidad Rey Juan Carlos, C/Tulipán s/n, 28933 Móstoles, Madrid, Spain. E-mail: isabel.hierro@urjc.es, yolanda.cortes@urjc.es*

[b] *Instituto de Investigación de Tecnologías para la Sostenibilidad, Universidad Rey Juan Carlos, Spain*

[c] *Advanced Porous Materials Unit, IMDEA Energy, Av. Ramón de la Sagra 3, 28935 Móstoles, Madrid, Spain*

† Electronic supplementary information (ESI) available. See DOI: **https://doi.org/10.1039/d4ew00410h**

respectively).[5] Rhodamine B (RhB), a carcinogenic dye, is commonly found in industrial wastewater (around 1.0 mg $L^{-1}$), provoking water colouring.[6] Therefore, these pollutants present a significant hazard to the environment and the depleting water reserves, projecting that approximately 1.8 billion people will face a lack of access to drinking water by 2030.[7] This situation urges the development of more effective and environmentally sustainable decontamination approaches. Among these methods, visible-light-driven heterogeneous photocatalysis has emerged as a highly promising and competitive technology.[8]

To fulfill this objective, bismuth-based photocatalysts are promising candidates owing to their impressive structural and optoelectronic properties, along with their appealing electronic structure.[9] Among them, $BiOCl_{1-x}I_x$ or $BiOBr_{1-x}I_x$ solid solutions may be excellent alternatives since they enhance the visible-light photocatalytic activity of the bismuth oxyhalide materials (*i.e.* BiOCl or BiOBr) while facilitating charge separation. For instance, Zhang *et al.*[10] studied the photocatalytic activity of various $BiOBr_xI_{1-x}$ solid solutions and found that $BiOBr_{0.8}I_{0.2}$ showed the highest performance in degrading RhB, due to its effective light absorption and suitable band arrangement. Kong *et al.*[11] also explored this set of solid solutions, demonstrating that $BiOBr_{0.75}I_{0.25}$ achieved better photoactivity in degrading RhB. $BiOBr_{0.5}I_{0.5}$ microspheres with highly exposed {1 1 0} facets were the most effective photocatalyst for degrading phenol.[12] Similarly, $BiOCl_xI_{1-x}$ ($x > 0.5$) have been efficiently used in the degradation of dyes. For example, $BiOCl_{0.75}I_{0.25}$ had the best adsorption and photocatalytic capacities for removing RhB[13] and $BiOCl_{0.6}I_{0.4}$ was effective in degrading acid red B.[14] Recently, Lu *et al.*[15] investigated how the compositions of bismuth oxybromide solid solutions affect the photocatalytic activity to individually degrade various model contaminants (including bisphenol A, tetracycline, malachite green, methyl violet and rhodamine B). They demonstrated that the degradation efficiency of the solid solution depends on its valence band potential, being slightly more positive than the oxidation potential of the contaminant. In this sense, most studies have focused on the removal of a single contaminant in distilled water, despite the fact that wastewater contain complex mixtures of contaminants,[16] as well as co-existing inorganic species (*i.e.* $HCO_3^-$, $NO_3^-$, $SO_4^{2-}$, $Cl^-$, $Na^+$, $Ca^{2+}$).[17] Thus, the identification of alternative pathways to enhance the ability of photocatalysts to resist interference from complex water matrices is imperative for their practical application. To date, there have been limited reports on the simultaneous photocatalytic removal of multiple organic contaminants and, predominantly relying on heterojunctions (*e.g.* 2D/2D $TiO_2$(B)–BiOBr and $TiO_2$-MIL-53(Al)).[18,19] To the best of our knowledge, no studies have yet reported on the simultaneous degradation of contaminant mixtures using bismuth oxyhalide solid solutions.

According with the positive outcomes using $Cl^-$ and $Br^-$ containing bismuth oxyhalide solid solutions, we propose the use of two optimal photoactive semiconductors, $BiOCl_{0.9}I_{0.1}$ and $BiOBr_{0.9}I_{0.1}$, as efficient visible-light harvesting photocatalysts for the simultaneous removal of three different kind of contaminants (*i.e.* CIP, MP and RhB). Additionally, we performed a comprehensive analysis of photocatalysts' band structure and charge separation–migration, and the oxidation potentials of the contaminants, through optical and solid-state electrochemical experiments.

## 2. Experimental section

### 2.1. Materials

Bismuth(III) nitrate pentahydrate ($Bi(NO_3)_3·5H_2O$, reagent grade), potassium iodide (KI, for analysis), potassium chloride (KCl, for analysis), and potassium bromide (KBr, for analysis) were purchased from Chem Lab, Fluka, Panreac, and Acros Organics, respectively. Ethylene glycol and ethanol were acquired from Glentham Life Sciences and VWR Chemical, respectively. Methyl 4-hydroxybenzoate (99%) and ciprofloxacin (98%) were purchased from Acros Organic and rhodamine B (>95%) and humic acid (HA) were purchased from Sigma. Sodium bicarbonate ($NaHCO_3$, Pharmpur®), sodium chloride (NaCl, synthesis grade), and sodium nitrate ($NaNO_3$, extra pure) were purchased from Scharlau, and sodium sulphate ($Na_2SO_4$, reagent grade) was purchased from Probus.

### 2.2. Synthesis of BiOX and $BiOX_{0.9}I_{0.1}$ materials

$BiOX_{0.9}I_{0.1}$ (X = Br, Cl) solid solutions were prepared following a previously reported method.[20] 6 mmol of $Bi(NO_3)_3·5H_2O$ was added to 44 mL of ethylene glycol. Subsequently, 44 mL of an aqueous solution of the correspondent potassium salt (0.13 M) was added dropwise, and the mixture was stirred for 3.5 h. The resulting yellow solids were filtered, washed with water and ethanol, and dried at 70 °C for 5 h. The resulting materials were denoted as $BiOCl_{0.9}I_{0.1}$ and $BiOBr_{0.9}I_{0.1}$ with a molar ratio of KCl/KI or KBr/KI of 0.9, respectively. For comparison purposes, BiOBr and BiOCl were also synthesized using the same procedure by adding the stoichiometric amounts of KBr and KCl (6 mmol each), respectively.

### 2.3. Characterization

X-Ray diffraction (XRD) patterns were obtained with a Phillips Diffractometer model PW3040/00 X'Pert MPD/MRD at 45 kV and 40 mA, with Cu-Kα radiation ($\lambda$ = 1.5418 Å). $N_2$ adsorption–desorption isotherms were acquired using a Micromeritics TriStar 3000 analyzer. FT-IR spectra were measured on a Spectrum Two FT-IR spectrometer Perking-Elmer equipped with an attenuated total reflectance (ATR) mode (in the region 4000 to 400 $cm^{-1}$). A Perkin Elmer 850 spectrophotometer in diffuse reflectance mode was employed to collect DRUV-vis spectra from 250 to 800 nm. For the morphological characterization, the materials were analysed using transmission electron microscopy (TEM) with a

PHILIPS TECNAI-10 electronic microscope at 200 kV and field-emission scanning electron microscopy (FESEM) using a JEOL (JSM 7900F) scanning microscope at an accelerating voltage of 10 kV. Photoluminescence (PL) spectra were collected with a Perkin Elmer Fluorescence spectrometer FL 8500, the materials were excited at a wavelength of 266 and 315 nm for bromide-containing or chloride-containing materials respectively, measuring emission from 300 to 500 nm. Electrochemical measurements were conducted on a potentiostat/galvanostat Autolab PSGTAT302 with modified carbon paste electrodes (MCPE) in a 0.2 M $Na_2SO_4$ solution in Milli-Q water. All the electrochemical measurements were conducted using a modified carbon paste electrode. This electrode contains a mixture of commercial carbon paste (Metrohm), the material in a 90–10% ratio and nujol as a binder. All the measurements (including cyclic voltammetry (CV), linear sweep voltammetry (LSV) and Mott–Schottky plots) were carried out using $Na_2SO_4$ (0.2 M) as the electrolyte, Ag/Ag/Cl/KCl as the reference electrode, and a platinum rod as the counter electrode, except for electrochemical impedance spectroscopy (EIS). For EIS measurements, KOH (0.1 M) was used as the electrolyte. All tests were carried out using an Autolab PSGTAT302 with an impedance module, and the software used was Nova 2.0. Photocurrent experiments utilized a commercial glassy carbon electrode. A composite ink, comprising the material and Ketjenblack carbon (3 mg of active material with 5 mg of graphite powder), was formulated in a 1 mL solution of absolute ethanol. Milli-Q water (1 : 1) and 20 μL of Nafion were added. The resulting ink was drop-casted onto the electrodes (6 μL) and allowed to air-dry. The experimental protocol consisted of three cycles, with 10-second intervals of darkness followed by 20-second exposure to light.

### 2.4. Photocatalytic degradation experiments

The activity of the photocatalysts was studied in the degradation of individual contaminants or mixtures of contaminants. Ciprofloxacin (CIP), methylparaben (MP) and rhodamine B (RhB) were selected as model recalcitrant contaminants. In a typical experiment, the photocatalyst (20 mg) was put in contact with 20 mL of an aqueous solution containing CIP (15 mg $L^{-1}$), MP (10 mg $L^{-1}$), or RhB (13 mg $L^{-1}$) or a mixture of the three contaminants. The mixture was stirred in darkness for 30 min to ensure adsorption–desorption equilibrium. Subsequently, the mixture was irradiated under visible light (300 W Xe lamp with a cut-off filter $\lambda > 420$) and aliquots of the mixture were taken and analysed at different time intervals. The concentrations of MP and CIP were calculated by HPLC analysis utilizing a C18 reverse-phase column (4.4 μm, 4.6 × 250 mm) and a UV detector. The mobile phase consisted of a mixture of methanol and water (30 : 70), delivered at a flow rate of 0.7 mL $mol^{-1}$. The detector wavelength was set to 272 and 256 nm for CIP and MP, respectively. The retention times were 2.89 min for CIP and 5.19 min for MP. The concentration of RhB was determined by UV-vis spectroscopy, monitoring the change in absorbance at 446 nm. LC-MS analysis was performed on a 1620 Infinity II HPLC system (Agilent Technologies), equipped with a PDA detector 1260 DAD HS and an API-Electrospray source (positive ion mode, mass scan range of from 50 to 500 *m*/*z*). The analysis was performed at 35 °C, with a flow rate of 0.3 mL $min^{-1}$, and using a InfinityLab Poroshell 120 EC-C18 column (2.1 × 50 mm; 2.7 Micron). The mobile phase was a linear gradient starting at 95% of aqueous solution (A) (0.1% formic acid): 5% of methanol (MeOH) from 0 to 5 min to a 5% A: 95% B from 5 to 10 minutes. The retention time was 4.4 min for CIP.

## 3. Results and discussion

### 3.1. Synthesis and characterization of the photocatalysts

BiOX and $BiOX_{0.9}I_{0.1}$ samples (X = Cl and Br) were synthesized following a facile precipitation procedure under mild conditions (*i.e.* room temperature and atmospheric pressure). The XRD patterns of the BiOCl and BiOBr samples show pure phases in both cases (Fig. S1†), while the diffractograms of the $BiOX_{0.9}I_{0.1}$ samples display peaks corresponding to tetragonal BiOCl (JCPDS 006-0249) for $BiOCl_{0.9}I_{0.1}$ and tetragonal BiOBr (JCPDS 01-078-0348) for $BiOBr_{0.9}I_{0.1}$ (Fig. 1a). No other peaks were observed in the diffractograms, indicating, therefore, the absence of the BiOI phase (Fig. S1†). Moreover, the diffraction peaks in the 25 to 35° region are shifted relative to the pure BiOCl and BiOBr phases (Fig. 1b). This shift is attributed to the increased lattice spacing resulting from substituting $Cl^-$ or $Br^-$ with $I^-$, which has a larger atomic radius (0.99 or 1.14 *vs.* 1.33 Å, respectively). This suggests that the $BiOX_{0.9}I_{0.1}$ samples are solid solutions.[21] As expected, the incorporation of iodine into the structure increases the *c*-unit cell parameter and the cell volume, since the halides are located between the $[Bi_2O_2]^{2+}$ layers, inducing an expansion in the crystal lattice (Table 1).[22] In addition, the incorporation of iodine reduces the crystallite sizes of the bismuth oxyhalide solid solutions, compared to pure BiOCl and BiOBr samples (Table 1).

The FTIR spectra of all prepared bismuth-based samples are displayed in Fig. S2.† In all the spectra, a band appears at around 500 $cm^{-1}$, which is attributed to the Bi–O bond. In addition, the vibrations related to the Bi–X bond are observed between 1000 and 1500 $cm^{-1}$.[23] Furthermore, the band associated with the O–Bi–O bond is observed at 874 $cm^{-1}$.[24] For $BiOX_{0.9}I_{0.1}$ samples, an additional band appears at 1366 $cm^{-1}$, which can be assigned to the stretching vibration of the Bi–I bond[25] (Fig. S2c†). Additionally, a band corresponding to the O–H bond is noticeable at around 1625 $cm^{-1}$, which is associated to the physiosorbed water.

The specific surface areas of the as-prepared bismuth-based materials were calculated from nitrogen adsorption/desorption isotherms (Fig. S3†), which are consistent with

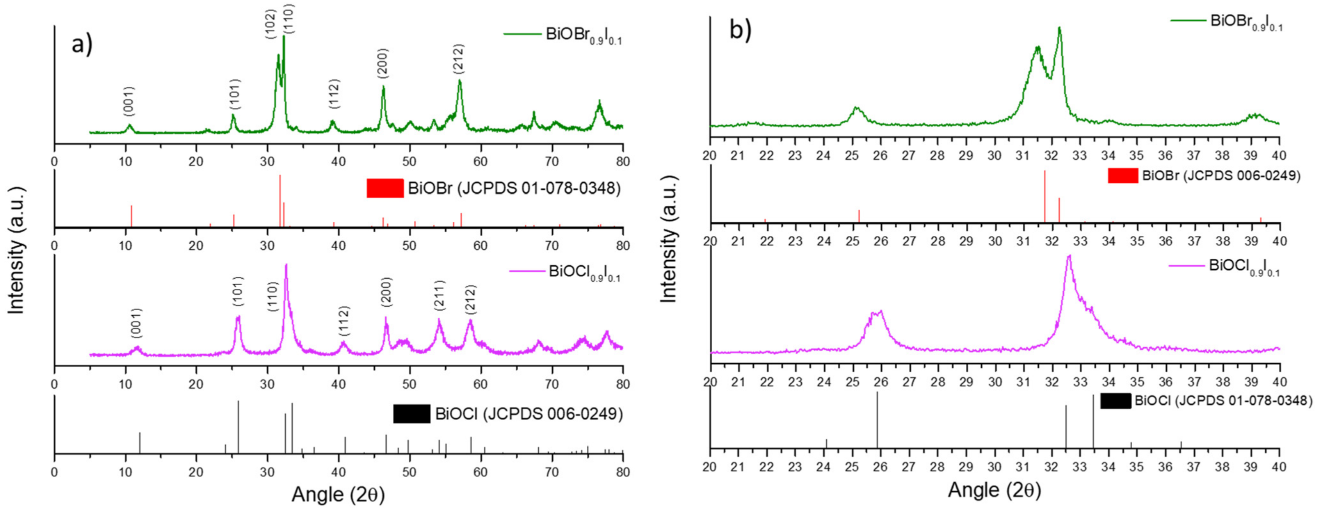

**Fig. 1** a) XRD patterns of the $BiOX_{0.9}I_{0.1}$ samples and the standard patterns of BiOBr and BiOCl and b) an expanded view of the diffraction patterns (region between 20° and 40°).

**Table 1** Specific surface areas ($S_{BET}$), pore volume ($V_p$), crystalline sizes, band gap values and lattice parameters for bismuth-based samples

| Material | $S_{BET}$ ($m^2$ $g^{-1}$) | $V_p$[a] ($cm^3$ $g^{-1}$) | Band gap[b] (eV) | Crystalline size[c] (nm) | Lattice parameters[d] | | |
|---|---|---|---|---|---|---|---|
| | | | | | $a = b$ (Å) | $c$ (Å) | $V$ ($Å^3$) |
| BiOBr | 18.4 | 0.076 | 2.77 | 54.21 | 3.92 | 8.10 | 124.52 |
| $BiOBr_{0.9}I_{0.1}$ | 17.6 | 0.090 | 2.37 | 49.88 | 3.92 | 8.21 | 126.36 |
| BiOCl | 23.7 | 0.074 | 3.47 | 25.75 | 3.88 | 7.38 | 111.28 |
| $BiOCl_{0.9}I_{0.1}$ | 21.1 | 0.097 | 2.45 | 25.33 | 3.88 | 7.49 | 113.77 |

[a] Pore volume calculated by the BJH method. [b] Estimated by Kubelka–Munk function. [c] Determined by Scherrer equation. [d] Calculated using Bragg's law for the diffraction peaks (110) and (102) for $BiOBr_{0.9}I_{0.1}$ and (110) and (101) for $BiOCl_{0.9}I_{0.1}$.

previous works.[13] As can be seen in Table 1, all the materials have comparable BET surface areas (ranging between 18–24 $m^2$ $g^{-1}$) and pore volumes (0.07–0.09 $cm^3$ $g^{-1}$), suggesting that the addition of iodine does not significantly influence the textural properties of the BiOX samples.

To complete the characterization of the materials, the electrochemical properties of $BiOCl_{0.9}I_{0.1}$ and $BiOBr_{0.9}I_{0.1}$ compared to BiOCl and BiOBr samples were examined. All these studies were conducted in the solid-state using carbon paste modified electrodes and employing cyclic voltammetry (CV). Scan ranges from 50 mV $s^{-1}$ to 150 mV $s^{-1}$ were examined, with increments of 25 mV $s^{-1}$. The study carried out for BiOBr is shown in Fig. 2a. The CV curve for BiOBr exhibits typical behavior for such materials, with signals present for the faradaic process of $Bi^{3+} \leftrightarrow Bi^0$. In the direct CV scan (towards negative potential values) (Fig. 2a), the primary cathodic peak at −0.9 V for 50 mV $s^{-1}$ is associated with the reduction of adsorbed $BiO_2^-$ species to Bi(0). These $BiO_2^-$ species are generated by the redissolution of Bi(III) species that are embedded in the crystalline structure and located on the electrode surface. In this regard, the reduction reaction to Bi(0) has been described as a series of consecutive reactions. Firstly, the dissolved $BiO_2^-$ species are reduced to $BiO_2^{2-}$, which is followed by the disproportionation of $BiO_2^{2-}$ to $BiO_2^-$ and Bi(0).[26] The higher the scan rate, the higher the current and the broader the peak, which also generates a slight shift towards negative potentials, as shown in Fig. 2a. Thus, the anodic peaks correspond to those found in the bibliography for the oxidation of Bi(0). The peak located at more negative potentials (−0.31 V at 50 mV $s^{-1}$) is attributed to the oxidation of Bi(0) located at the solution–surface interface to Bi(III) and the peak at a positive potential (0.13 V at 50 mV $s^{-1}$) is associated with the oxidation of Bi(0) to Bi(III). The mechanism of the formation of Bi(III) firstly involves the formation of Bi(I), followed by its disproportionation to Bi(III) and Bi(0).[27]

As can be seen in Fig. 2b–d, all other studied materials display similar anodic behavior in CV, with consistent signals attributed to Bi(0) oxidation, when scanned towards positive potentials. In the cathodic part of the CV, significant changes are observed in the reduction peak value. These changes can be due to the different chemical environments for Bi(III) species, which influence their electrochemical behavior. The cathodic peak for BiOCl is observed at −0.74 V (Fig. 2c), which is at a higher

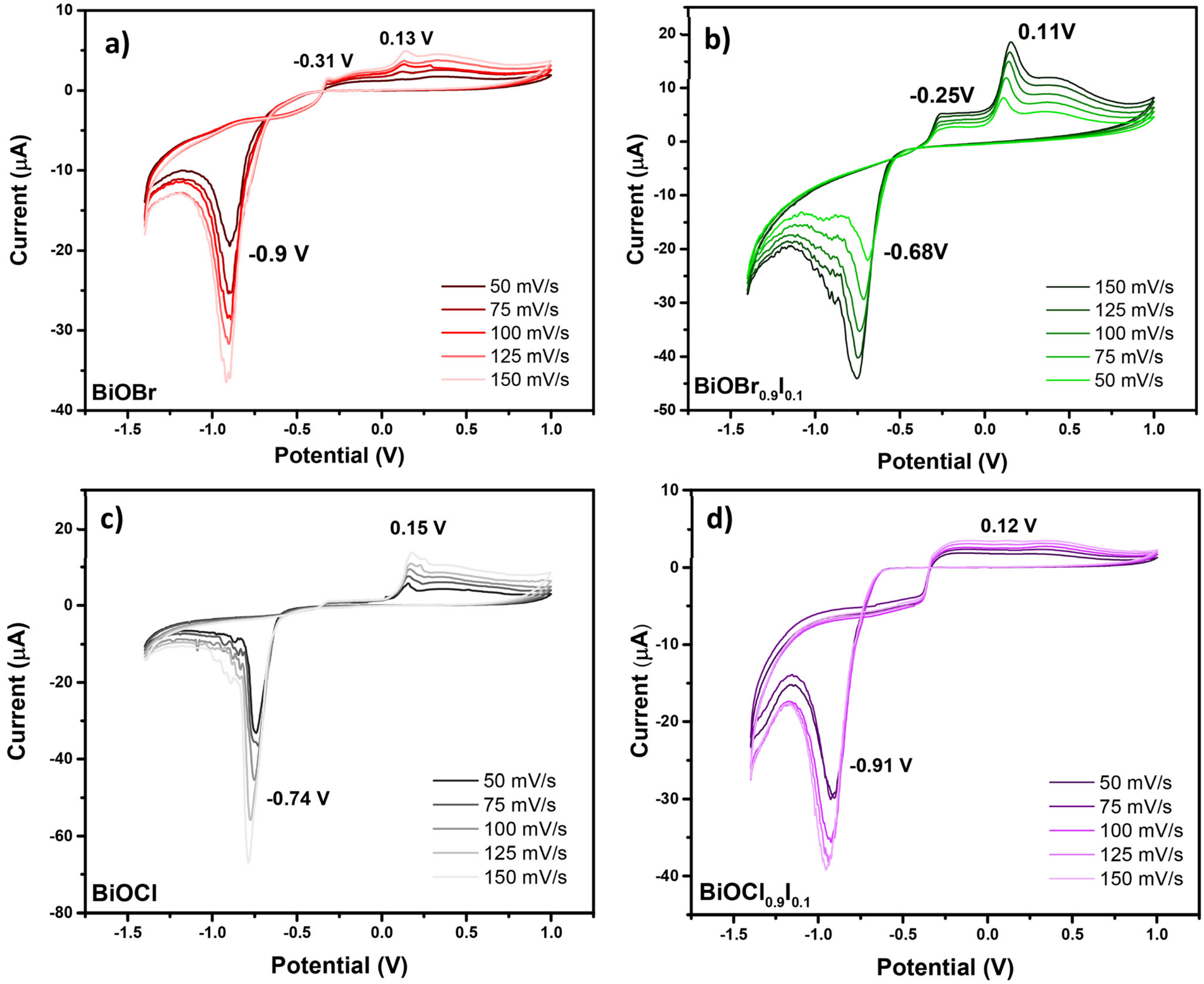

Fig. 2 CV of a) BiOBr b) $BiOBr_{0.9}I_{0.1}$ c) BiOCl and d) $BiOCl_{0.9}I_{0.1}$ carbon modified electrode as a working electrode in 0.2 M $Na_2SO_4$ (potential (V) *vs.* Ag/AgCl/KCl) with a platinum rod as a counter electrode (measured from 1 to −1.4 V).

potential (less negative) than that of BiOBr. In layered materials (*i.e.* BiOX), Bi(III) species are known to be embedded in $BiO_2^{2+}$ layers, which are bound by corresponding anion layers (X = Cl, Br, I). These anions have different electronegativities, thus affecting the charge over the Bi(III) species differently depending on halide. The higher electronegativity of $Cl^-$ results in a higher electron withdrawal effect over Bi(III) species, causing a shift of the cathodic potential to −0.74 V.

Similarly, the introduction of iodine into the interlayer ($BiOCl_{0.9}I_{0.1}$) causes a potential shift from −0.74 to −0.91 V (Fig. 2c and d), which can be explained by its lower electronegativity. Unexpectedly, in the $BiOBr_{0.9}I_{0.1}$ material, the introduction of $I^-$ causes a shift from −0.9 to −0.68 V (Fig. 2a and b), which suggests that other factors than electronegativity are influencing the electrochemical behavior of these Bi(III) species. The electrochemical characteristics can tentatively be attributed to the synergistic effects between the $[BiO_2]^{2+}$ layers and the $X^-$ anion, which influence the electrical conductivity and the chemical properties of the active centers. The presence of Bi(III) species in the framework, with Lewis acid properties, may significantly enhance its adsorptive properties towards pollutants. Additionally, the presence of $X^-$ anion may influence their electrical conductivity, as demonstrated by the photocurrent density studies (see Fig. 7).

Field emission scanning electron microscopy (FESEM) analysis revealed the layered morphology of the bismuth oxyhalide solid solutions (Fig. 3), which form flower-like particles composed of nanosheets, as confirmed by transmission electron microscopy (TEM) analysis (Fig. S4†). In addition, scanning electron microscopy-energy dispersive X-ray (SEMEDX) mapping disclosed a uniform distribution of Bi, O, I, Cl and Br elements on the flower-like particles (Fig. S5 and S6†).

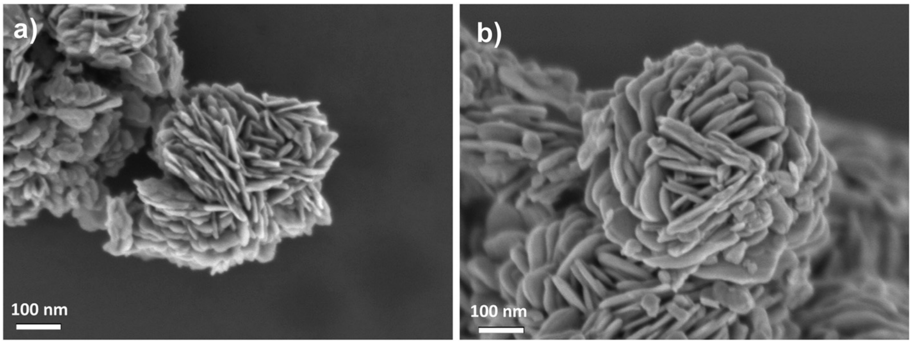

**Fig. 3** FESEM images of a) $BiOCl_{0.9}I_{0.1}$ and b) $BiOBr_{0.9}I_{0.1}$.

The absorption ability was investigated by UV-vis diffuse reflectance (DRUV-vis). As illustrated in Fig. 4a, BiOCl and BiOBr samples display reduced visible absorption, while the absorption edges of $BiOCl_{0.9}I_{0.1}$ and $BiOBr_{0.9}I_{0.1}$ are red-shifted, with the $BiOBr_{0.9}I_{0.1}$ sample showing a stronger response to visible light. Consequently, the band gap values of the samples were calculated by Kubelka–Munk transformation[28] (Fig. 4b), assuming an indirect band gap transition since BiOCl and BiOBr are indirect band gap semiconductors.[29] As a result of incorporation of iodine, the band gap values of BiOCl and

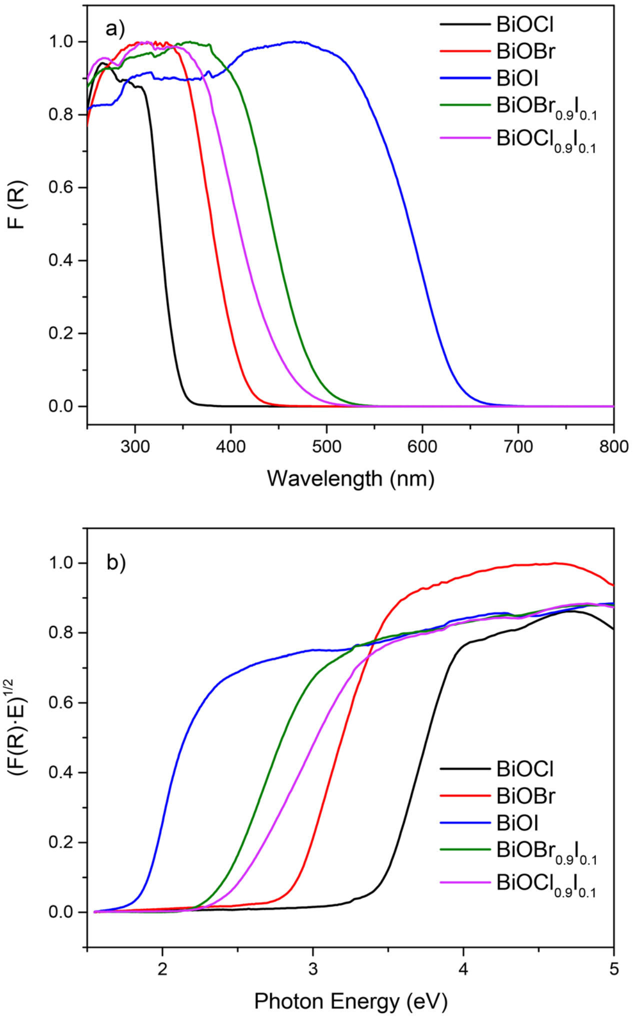

**Fig. 4** a) DRUV-vis spectra and b) plots of transformed Kubelka–Munk function *vs.* photon energy (eV) of bismuth-based materials.

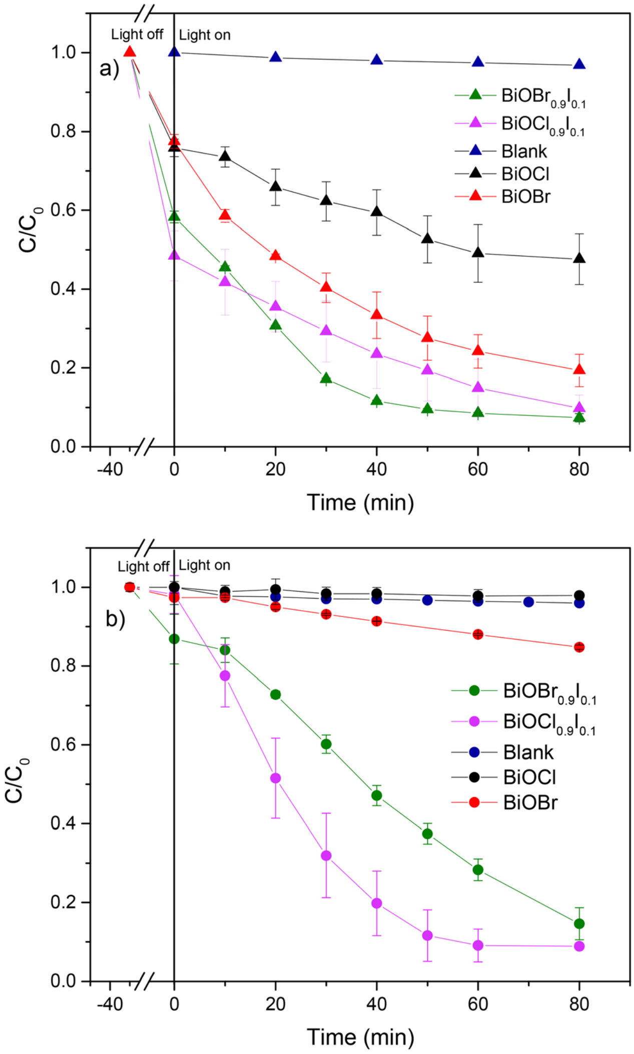

**Fig. 5** Photocatalytic degradation of a) CIP and b) MP using the as-prepared bismuth-based materials.

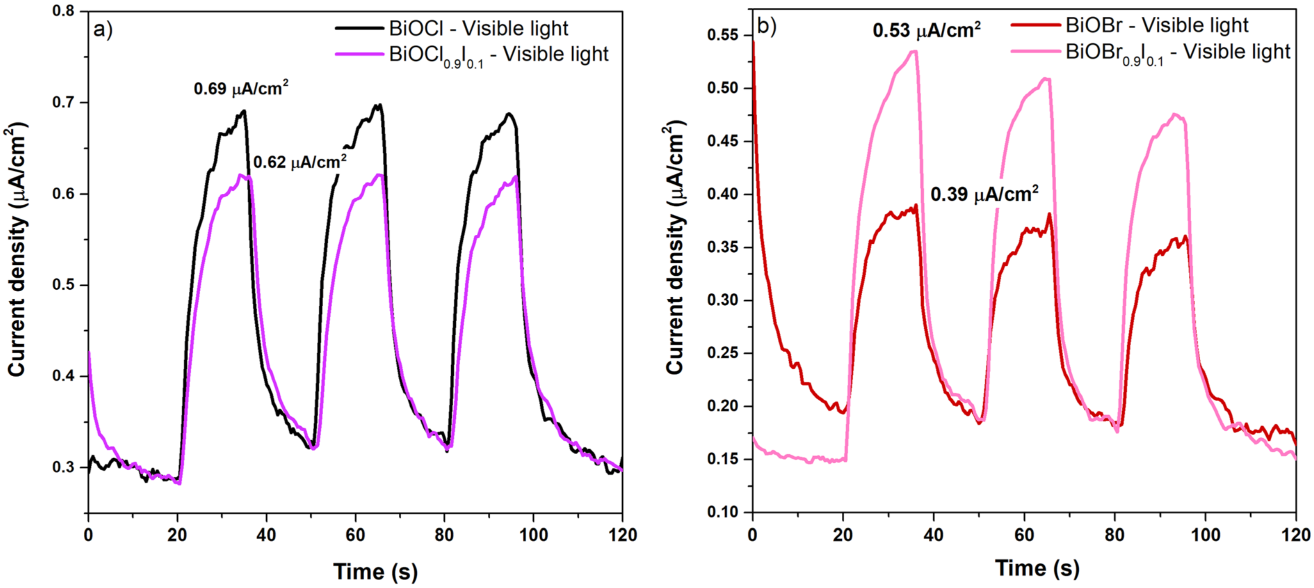

**Fig. 6** Photocurrent density of bismuth oxychloride-based samples (a) and bismuth oxybromide-based samples (b) at a potential of 1.0 V (V *vs.* Ag/AgCl) under visible light ($\lambda > 400$ nm).

BiOBr decrease significantly, from 3.47 eV for BiOCl to 2.45 eV for $BiOCl_{0.9}I_{0.1}$, and from 2.77 to 2.37 eV for BiOBr and $BiOBr_{0.9}I_{0.1}$, respectively.

### 3.2. Photocatalytic performance of the bismuth-based photocatalysts for CIP and MP degradation

Initially, we assessed the photocatalytic activity of the samples for the degradation of CIP and MP separately under visible light irradiation. As shown in Fig. 5, the blank samples of CIP and MP showed negligible degradation, highlighting that light alone is insufficient for degrading the CIP and MP molecules. Nevertheless, in the presence of bismuth-based photocatalysts, $BiOX_{0.9}I_{0.1}$ samples were able to remove CIP more efficiently (>90% in 80 min) than BiOBr (80.6% in 80 min) and BiOCl (52.4% in 80 min) (Fig. 5a). It is important to note that for MP removal, BiOBr and BiOCl samples exhibited very poor efficiency (15% and 2%, respectively), while $BiOX_{0.9}I_{0.1}$ samples effectively degraded MP (91.1% and 85.4% in 80 min for $BiOCl_{0.9}I_{0.1}$ and $BiOBr_{0.9}I_{0.1}$, respectively) (Fig. 5b). All kinetics followed a pseudo-first order degradation (Fig. S7†), where the highest $k$ values were achieved by $BiOCl_{0.9}I_{0.1}$ for the MP degradation ($k$ = 0.037 $min^{-1}$), and $BiOBr_{0.9}I_{0.1}$ for the CIP degradation ($k$ = 0.035 $min^{-1}$). These $k$ values are higher than those found using other Bi-containing systems (Table S1†) – including Bi-based composites $Fe_2O_3/BiVO_3$/biochar assembly,[30] $BiOBr/Bi_4O_5Br_2$,[31] 3%$BiVO_4/TiO_2$,[32] $BiVO_4$/Ag/$MnO_2$,[33] or Ag–$BiVO_4$[34] and comparable with that of the iodine-doped photocatalyst, $I_{1.0}$–$Bi_4O_5Br_2$ ($k$ = 0.0368 $min^{-1}$ for MP degradation).[35]

The superior performance of $BiOX_{0.9}I_{0.1}$ solid solutions in degrading CIP and MP under visible light irradiation could be attributed to the enhanced separation and migration efficiency of photogenerated charges, which were evaluated using photoluminescence (PL) spectroscopy and photocurrent response. PL spectra were obtained by exciting the BiOBr-based and BiOCl-based samples at 266 and 315 nm, respectively (Fig. S8†). Both $BiOCl_{0.9}I_{0.1}$ and $BiOBr_{0.9}I_{0.1}$ samples show PL bands with significantly lower intensity than those observed for BiOCl and BiOBr samples. This indicates that the I-modified samples exhibit less recombination of photoinduced electron–hole pairs, a key factor for a promising photocatalyst. Furthermore, $BiOBr_{0.9}I_{0.1}$ shows a notably higher photocurrent density than BiOBr (0.53 *vs.* 0.39 µA $cm^{-2}$) (Fig. 6a). However, this value is surpassed by bismuth oxychloride-based samples, which are 0.62 and 0.69 µA $cm^{-2}$ for $BiOCl_{0.9}I_{0.1}$ and BiOCl, respectively (Fig. 6b), indicating that $BiOCl_{0.9}I_{0.1}$ is the most efficient in generating and migrating charge carries compared to BiOBr and $BiOBr_{0.9}I_{0.1}$.

To gain additional insights into the superior photocatalytic performance of $BiOCl_{0.9}I_{0.1}$, XPS measurements were conducted for $BiOCl_{0.9}I_{0.1}$ and BiOCl, the latter for reference and comparison purposes. The spectra were calibrated using the C 1s peak at 284.8 eV, which is attributed to the indefinite hydrocarbon produced by the XPS instrument. As expected, both XPS survey spectra (Fig. S9†) display signals corresponding to the C, O, Cl and Bi elements. The XPS spectrum of $BiOCl_{0.9}I_{0.1}$ exhibits two extra signals at 630.4 (I $3d_{3/2}$) and 618.9 eV (I $3d_{5/2}$), which are attributed to the presence of iodine, confirming the presence of $I^-$ atoms into the BiOCl structure. In the Bi signals (Fig. 7a), the binding energies of the doublet Bi $4f_{5/2}$ and Bi $4f_{7/2}$ in the spectrum of BiOCl are located at 164.9 and 159.5 eV, respectively, separated by 5.3 eV, indicating the characteristic Bi(III) oxidation state. It is worth noting that a negative shift of the Bi peaks (0.3 eV) is observed in the $BiOCl_{0.9}I_{0.1}$ sample, attributed to the presence of iodine atoms, which indicates

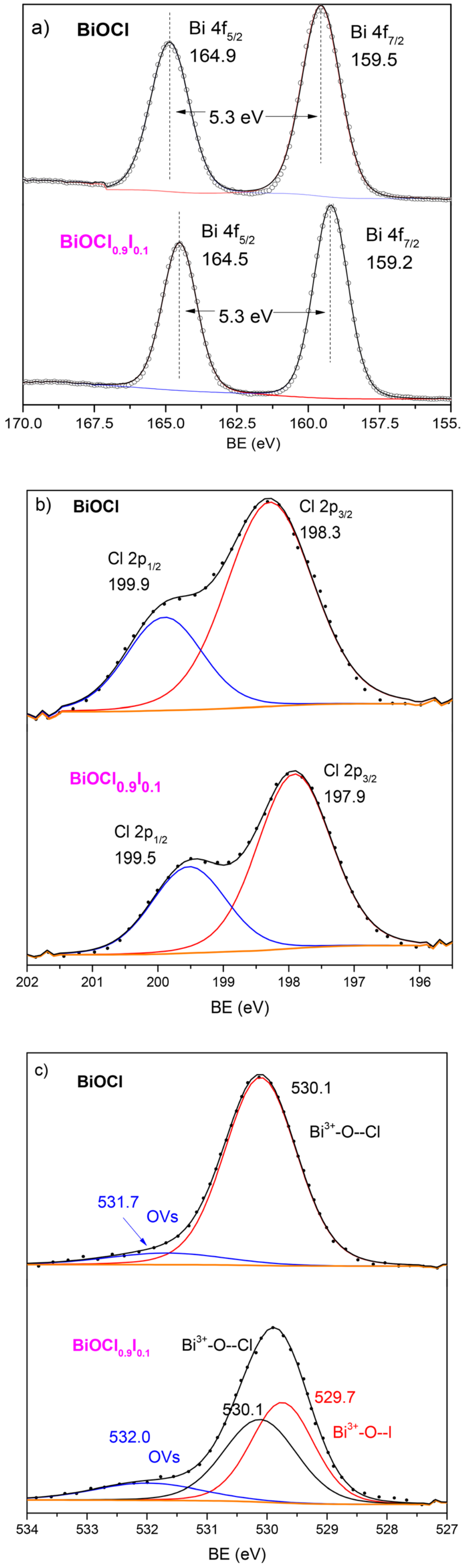

Fig. 7 XPS spectra of bismuth oxychloride-based samples a) Bi 4f, b) Cl 2p and c) O 1s regions.

an increase in the outer electron cloud density around Bi atom after iodine incorporation.[36] The Cl 2p spectra (Fig. 7b) show the same shift, with the Cl 2p$_{1/2}$ and Cl 2p$_{3/2}$ peaks in the BiOCl$_{0.9}$I$_{0.1}$ spectrum located at 199.5 and 197.9 eV, while in the BiOCl spectrum these peaks appear at 199.9 and 198.3 eV, corresponding to Cl$^{-}$ atoms. The O 1s signals for both materials (Fig. 7c) can be deconvoluted in two peaks at 530.1 and ~532 eV, attributed to lattice oxygen (Bi$^{3+}$–O–Cl) and oxygen vacancies (OVs), respectively. Although some authors have assigned this latter peak (~532 eV) to the O–H bond from the H$_2$O adsorbed on the surface, the absence of a significant signal for H$_2$O(l) (~533 eV) suggests that the peak at ~532 eV corresponds to oxygen vacancies.[37] In this regard, the concentration of oxygen vacancies is significant higher in BiOCl$_{0.9}$I$_{0.1}$ (13.1%) than in BiOCl (9.2%).[38] The increased OVs in the BiOCl$_{0.9}$I$_{0.1}$ sample could be beneficial for pollutant degradation, allowing to capture photogenerated electrons and reducing electron–hole recombination.[39]

### 3.3. Photocatalytic performance of bismuth-based photocatalysts in binary- and ternary systems of coexisting contaminants

The main goal of this study is to evaluate the photocatalytic activity of BiOX$_{0.9}$I$_{0.1}$ catalysts in the presence of multiple coexisting contaminants. Our focus is to examine the potential influence of a mixture of contaminants on the degradation process, aiming to identify synergistic effects that could enhance the elimination process, particularly within the context of specific types of polluted waters. In previous studies, Cherifi *et al.*[40] reported the simultaneous removal of Cr(VI) and phenol and identified Cr(VI) as an electron trap that promotes the phenol degradation and Han *et al.*[41] discovered that indirect RhB sensitization on the photocatalyst allows for the generation of a large amount of superoxide radicals during the degradation process, thereby enhancing the degradation efficiency. In this work, the simultaneous photocatalytic degradation of a mixture of CIP, MP and RhB was accomplished using both BiOX$_{0.9}$I$_{0.1}$ catalysts under visible light irradiation (Fig. 8). Outstandingly, the BiOCl$_{0.9}$I$_{0.1}$ photocatalyst completely eliminated RhB in 10 min and CIP in 40 min and degraded 86% of MP in 40 min (Fig. 8a). BiOBr$_{0.9}$I$_{0.1}$ also achieved total elimination of RhB in 10 min although requiring a longer time period (60 min) to degrade 98.5% and 87.1% of CIP and MP, respectively (Fig. 8b). Notably, both photocatalysts demonstrated superior performance in removing the mixtures of contaminants compared to eliminating the studied individual contaminants.

To gain a better understanding of the simultaneous degradation process by the most active BiOCl$_{0.9}$I$_{0.1}$ photocatalyst, the removal efficiencies of CIP and MP were compared in a single-, binary- (CIP/MP) and ternary-(CIP/MP/RhB) contaminant systems. For the CIP degradation in the presence of MP and RhB (ternary-contaminant system), the kinetic constant was 0.2 min$^{-1}$, which is 2.5 and 10 times

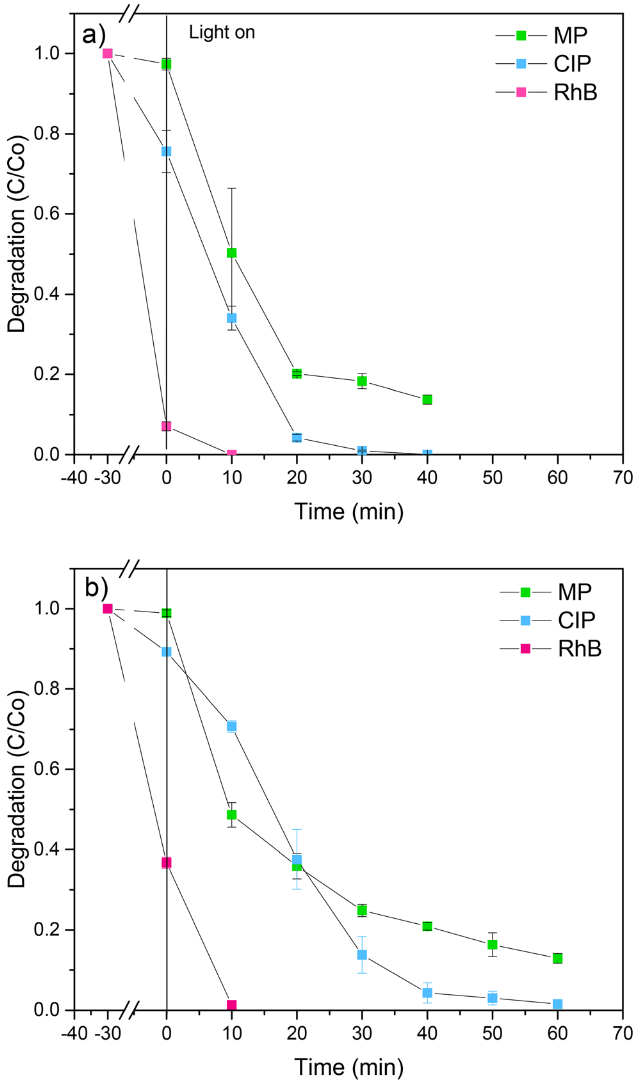

**Fig. 8** Simultaneous photodegradation of a mixture of MP, CIP and RhB using a) $BiOCl_{0.9}I_{0.1}$ and b) $BiOBr_{0.9}I_{0.1}$ samples.

higher than those obtained in the presence of only MP (binary system with $k = 0.08$ $min^{-1}$) and in the absence of MP and RhB (single system with $k = 0.02$ $min^{-1}$), respectively (Fig. S10a†). This behaviour suggests that the CIP removal efficiency of $BiOCl_{0.9}I_{0.1}$ is synergistic enhanced by the presence of both contaminants, MP and RhB. It is known that the degradation of MP promotes the generation of ROS, mainly hydroxyl radicals,[42] which could attack the CIP molecule, favoring its degradation. Meanwhile, RhB may serve as a source of superoxide radicals, enhancing the degradation process. In the case of MP degradation (Fig. S10b†), the $k$ values were 0.037, 0.021 and 0.049 $min^{-1}$ for the single-, binary- and ternary-pollutant systems, respectively. Thus, the presence of CIP reduces the degradation of MP, while the addition of RhB improves the MP degradation process. This could be due to the higher adsorption capacity of $BiOCl_{0.9}I_{0.1}$ for CIP compared to MP which results in a competitive effect that slows down the degradation of MP.

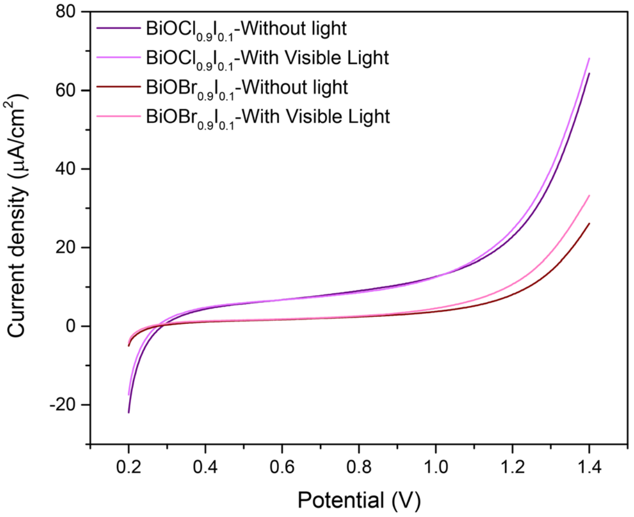

**Fig. 9** Linear sweep voltammetry of $BiOCl_{0.9}I_{0.1}$ and $BiOBr_{0.9}I_{0.1}$ samples from 0.2 to 1.4 V (*vs.* Ag/AgCl) under no light or visible light.

To gain additional insights into the superior photocatalytic performance of $BiOCl_{0.9}I_{0.1}$, the electron transfer efficiency and photo-response for the solid solutions were investigated by electrochemical impedance spectroscopy (EIS) (Fig. S11†) and linear sweep voltammetry (LSV) (Fig. 9) measurements, respectively. The Nyquist diagram indicates that the $BiOCl_{0.9}I_{0.1}$ sample has a superior transfer ability, as evidenced by its smaller semicircle radius compared to the $BiOBr_{0.9}I_{0.1}$ sample. Moreover, an equivalent Randles model circuit was fitted to the curves, demonstrating its efficacy in modeling both samples (see Fig. S11†). The circuit elements represent the system's resistance ($R_s$), attributed to the conductivity of the carbon paste mixture, the interconnections of all electrodes in the cell, and the characteristics and conductivity of the electrolyte. The other resistance ($R_p$) could be attributed to the material exhibiting the faradaic response (*i.e.* $BiOBr_{0.9}I_{0.1}$ or $BiOCl_{0.9}I_{0.1}$). The constant phase element (CPE) is employed to characterize the non-ideal capacitance arising from the surface roughness, porosity, and non-uniformity (Table S2†). The $R_p$ values are recorded at 23.2 and 35.3 kΩ for $BiOCl_{0.9}I_{0.1}$ and $BiOBr_{0.9}I_{0.1}$, respectively. This observation implies a lower resistance to ion conductivity for $BiOCl_{0.9}I_{0.1}$, potentially contributing significantly to its enhanced photocatalytic activity. Finally, LSV curves (Fig. 9) reveal that $BiOCl_{0.9}I_{0.1}$ generates the highest photocurrent density (applying a potential range of 0.2–1.4 V), indicating the highest photo-response to produce charge carriers. These results are consistent with the superior photocatalytic activity of $BiOCl_{0.9}I_{0.1}$ in degrading the mixture of contaminants.

### 3.4. Scavenger studies

To investigate the mechanism degradation process by $BiOCl_{0.9}I_{0.1}$, experiments using different scavenger were performed for MP and CIP degradation in the ternary-contaminant system. Thus, benzoquinone, ascorbic acid and isopropanol were employed as scavenger agents to trap superoxide radicals ($O_2^{\bullet-}$), positive holes ($h^+$) and hydroxyl radicals ($^{\bullet}OH$), respectively (Fig. S12†). The photodegradation of MP experienced a reduction to 4% and 24% in the presence of benzoquinone and ascorbic acid, respectively, while isopropanol had no significant effect on the process (Fig. S12a†). Consequently, superoxide radicals emerged as the primary active species participating in the photocatalytic reaction, which positive holes also playing an active role as secondary reactive species. This observation aligns with the energy band calculations for $BiOCl_{0.9}I_{0.1}$ (see Fig. 11). Similar outcomes were noted in MP degradation during trapping experiments were conducted for the mixed CIP/MP/RhB system (Fig. S12b†). These results confirmed $O_2^{\bullet-}$ and $h^+$ as the primary and secondary reactive species, respectively. It is noteworthy that the presence of the trapping agents $O_2^{\bullet-}$ and $h^+$ in the single system impacted more significantly the MP degradation, as observed by comparing the degradation values obtained in both experiments (4 and 24% *vs.* 18 and 37%). This is in alignment with the improvement in the degradation process due to the presence of RhB, which acts as a source of superoxide radicals. For the CIP degradation (Fig. S12c†), only the presence of benzoquinone shows a significant reduction of the photodegradation to 78%, whereas a not relevant 3% drop in photodegradation was observed when both isopropanol and benzoquinone were present. While the impact is somewhat less pronounced in the case of CIP, the observed trend aligns with that noted for MP, providing experimental confirmation that $O_2^{\bullet-}$ serves as the primary species involved in the process.

### 3.5. Mott–Schottky plots and energy band structure

Mott–Schottky plots were measured within a range −0.8 to 1.0 V in a 0.2 M $Na_2SO_4$ aqueous solution and recorded at 0.5 kHz (Fig. 10). Both materials showed positive slopes, indicating that they are n-type semiconductors, as previously described in the literature.[43] The energy band positions of the materials were estimated using the flat-band potential, which was determined from the intersection of the Mott–Schottky plot slope with the *x*-axis. As a result, $BiOCl_{0.9}I_{0.1}$ and $BiOBr_{0.9}I_{0.1}$ displayed similar values of −1.36 and −1.26 V *vs.* Ag/AgCl (−1.16 and −1.06 V *vs.* NHE), respectively. For n-type semiconductors, the conduction band ($E_{CB}$) is closely aligned with the flat band potential. Consequently, the $E_{CB}$ values obtained for $BiOCl_{0.9}I_{0.1}$ and $BiOBr_{0.9}I_{0.1}$ are −1.06 and −0.96 eV *vs.* NHE, respectively.[44] The valence band ($E_{VB}$) can be calculated from $E_{CB}$ and $E_g$ using the following equation:

$$E_{CB} = E_{VB} - E_g$$

where $E_g$ represents the band gap value estimated from the DRUV-vis spectra, yielding 2.45 eV for $BiOCl_{0.9}I_{0.1}$ and 2.37 eV for $BiOBr_{0.9}I_{0.1}$. Therefore, the calculated $E_{VB}$ values were 1.39 V for $BiOCl_{0.9}I_{0.1}$ and 1.41 V for $BiOBr_{0.9}I_{0.1}$. To confirm the calculated $E_{VB}$ values, the valence band potential ($E_{VB\text{-}XPS}$) of $BiOCl_{0.9}I_{0.1}$ was determined by XPS, as a

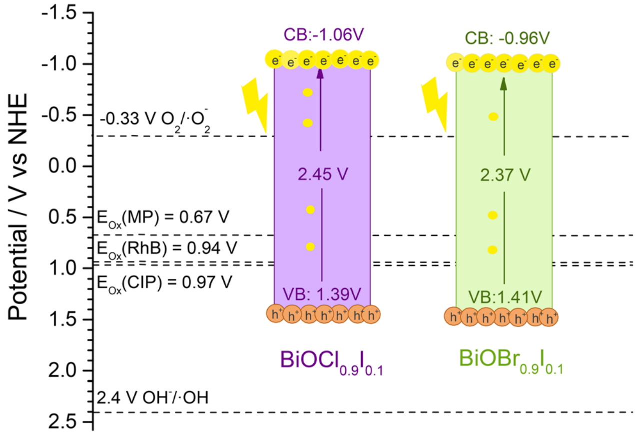

**Fig. 11** The band positions of $BiOCl_{0.9}I_{0.1}$ and $BiOBr_{0.9}I_{0.1}$ samples and the onset oxidation potentials ($E_{ox}$) of RhB, CIP and MP.

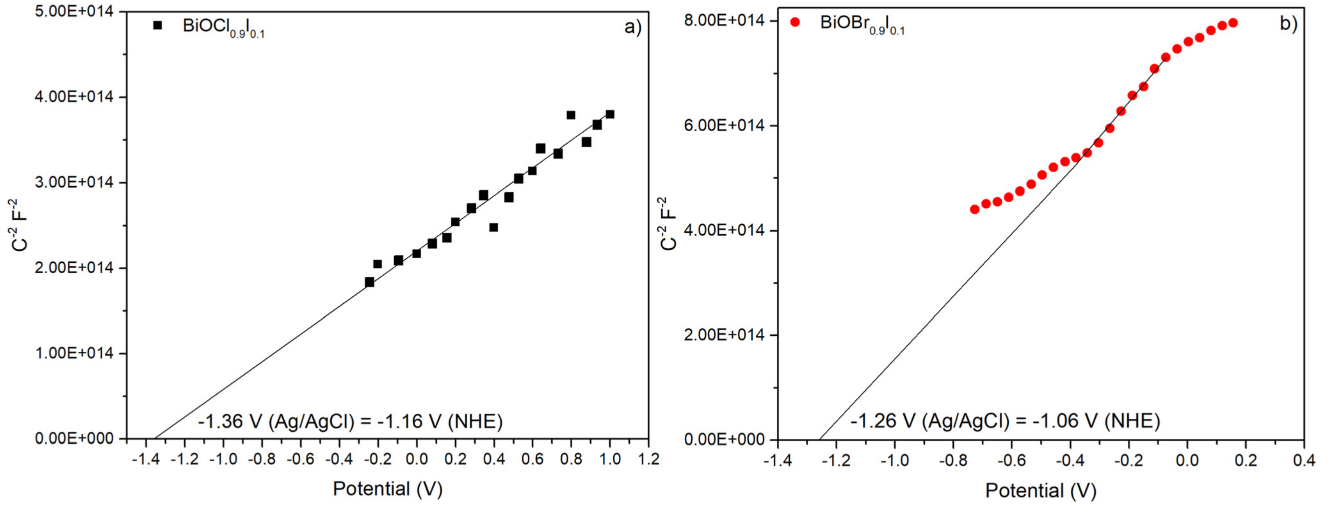

**Fig. 10** Mott–Schottky plots of a) $BiOCl_{0.9}I_{0.1}$ and b) $BiOBr_{0.9}I_{0.1}$ samples.

representative example. Thus, the $E_{\text{VB-XPS}}$ of $BiOCl_{0.9}I_{0.1}$ is 1.34 eV, according to the linear extrapolation method (Fig. S13†). Therefore, the corresponding $E_{\text{VB}}$ of $BiOCl_{0.9}I_{0.1}$ is 1.45 V ($E_{\text{VB}} = \varphi + E_{\text{VB-XPS}} - 4.44$, where $\varphi$ is the electron work function of the XPS instrument (4.55 eV)),[45,46] which is in concordance with the value obtained from Mott–Schottky (1.45 *vs.* 1.39 V). As observed in Fig. 11, the band positions of both solid solutions could only facilitate the generation of the superoxide radicals. Additionally, using Mott–Schottky plots the donor concentrations for both n-type semiconductors were estimated from the following equation:

$$\frac{1}{C^2} = \frac{2}{\varepsilon\varepsilon_{\text{o}}A^2eN_{\text{D}}}\left(V - V_{\text{fb}} - \frac{K_{\text{B}}T}{e}\right)$$

where $\frac{2}{\varepsilon\varepsilon_{\text{o}}A^2eN_{\text{D}}}$ is the slope, $A$ the area of the electrode, $e$ the charge of the electrode, $\varepsilon$ the relative permittivity constant $\varepsilon_{\text{o}}$ the dielectric constant,[47] and $N_{\text{D}}$ is the donor concentration per unit volume ($cm^{-3}$). As can be seen in the Table 2, $BiOCl_{0.9}I_{0.1}$ has a higher donor concentration compared to $BiOBr0._{9}I_{0.1}$ ($1.06 \times 10^{18}$ $cm^{-3}$ *vs.* $2.97 \times 10^{17}$ $cm^{-3}$, respectively), resulting in an enhanced electronic properties.[48]

As mentioned earlier, the photocatalytic process occurs when the absorption of visible light photons induces the promotion of electrons from the valence band to the conduction band, leading to the generation of ROS and holes. These entities play a crucial role in initiating the oxidation of pollutants, such as those examined in this study. To facilitate this process, it is imperative that the oxidation potential of the photogenerated holes ($h^+$) surpasses the oxidation potential of the pollutants.[49] Since $h^+$ are active species in the photodegradation process, a more positive $E_{\text{VB}}$ (*vs.* NHE) than the oxidation potential of the pollutant is a requirement for initiating its photodegradation. This value can be obtained by measuring the cyclic voltammograms of the pollutants and analyzing the oxidation and reduction peaks. The results are shown in Fig. S14,† which shows a distinct oxidation peak in all molecules, located around 1.16, 1.3 and 1.5 V *vs.* NHE for RhB, CIP, and MP, respectively. Thus, the onset oxidation potentials ($E_{\text{ox}}$) are obtained by extrapolation of the peak tangent line to $y = 0$, being 0.94, 0.97, and 0.67 V *vs.* NHE for RhB, CIP, and MP, respectively. These oxidation potentials are located between the valence and conduction bands of both $BiOCl_{0.9}I_{0.1}$ and $BiOBr_{0.9}I_{0.4}$ materials (see Fig. 11) and justify their ability to photodegrade the selected pollutants.

**Table 2** Slope and donor concentration ($N_{\text{D}}$) obtained from Mott–Schottky plots for bismuth-based samples

| Photocatalyst | Slope | $N_{\text{D}}$ ($cm^{-3}$) |
|---|---|---|
| $BiOCl_{0.9}I_{0.1}$ | $1.62 \times 10^{14}$ | $1.06 \times 10^{18}$ |
| $BiOBr_{0.9}I_{0.1}$ | $6.62 \times 10^{14}$ | $2.97 \times 10^{17}$ |

### 3.6. Photocatalytic performance of bismuth-based photocatalysts in ternary systems of coexisting contaminant under more realistic conditions

To further test the applicability of $BiOCl_{0.9}I_{0.1}$ in realistic water conditions, the impact of inorganic anions and organic matter, and the use of tap water on the degradation was studied in the mixed CIP/MP/RhB system under visible light irradiation. Humic acid (HA), a natural component found in the range from 0.1 to 10 mg $L^{-1}$,[50] was selected for this study at a concentration of 1 mg $L^{-1}$. For inorganic species, $HCO_3^-$, $Cl^-$, $NO_3^-$, and $SO_4^{2-}$ were selected and tested at a concentration of 0.5 mM.[51] All these anions have been described as scavengers of reactive radical species, which is associated with a significant decrease of the photocatalytic degradation activity.[52] As can be seen in Fig. 12a, the effect of the inorganic ions varies significantly depending on the pollutant. For the degradation of RhB, no diminishing effect was observed, achieving 100% degradation. This could be due to the high adsorption capacity of $BiOCl_{0.9}I_{0.1}$ for RhB (>90%, Fig. 8a), which could ensure contact between the photocatalyst and the pollutant, thereby eliminating the possible effect of the presence of anions. This trend was maintained in all experiments (see Fig. 12a). CIP removal slightly decreased to 94.2%, 92.5% 91.8% and 91.3% in presence of $HCO_3^-$, $Cl^-$, $SO_4^{2-}$ and $NO_3^-$, respectively, supporting the better photocatalytic performance of $BiOCl_{0.9}I_{0.1}$ for CIP compared to MP in the mixed CIP/MP/RhB system (Fig. 8a). For MP, the effect of inorganic ions on the degradation process was more pronounced, achieving less than 75% ($HCO_3^- < SO_4^{2-} < NO_3^- < Cl^-$, $72.9\% < 67.3\% < 64.2\% < 54.3\%$, respectively) (Fig. 12a). For example, $NO_3^-$ reacts with $h^+$ to generate $NO_3\cdot$ radicals, acting as a scavenger for $h^+$.[53] As mentioned, the presence of scavengers has a more significant impact on the degradation of MP compared to CIP (Fig. S12b *vs.* c†). This supports the fact that the presence of inorganic species can hinder the MP degradation. When the photodegradation was performed in the presence of HA or tap water (Fig. 12b), a similar behaviour was observed. The degradation efficiency of RhB was maintained (100%), while CIP removal suffered a slight decrease (91.4% and 91.7% for HA and tap water, respectively), and MP degradation significantly diminished (60.7% and 63.6% for HA and tap water, respectively). Despite a slight reduction on photodegradation potential when utilizing the studied material in realistic water conditions, $BiOCl_{0.9}I_{0.1}$ exhibited a highly attractive behavior, validating the study of its degradation mechanism as well as its plausible applicability in treating real water samples containing mixtures of different contaminants including rhodamine B, before potential human use.

### 3.7. Degradation mechanism of CIP and toxicity of degradation intermediates

As mentioned above, $BiOCl_{0.9}I_{0.1}$ has high potential in photodegradation of waters with mixtures of contaminants, in addition, the CIP degradation by $BiOCl_{0.9}I_{0.1}$ suffers a

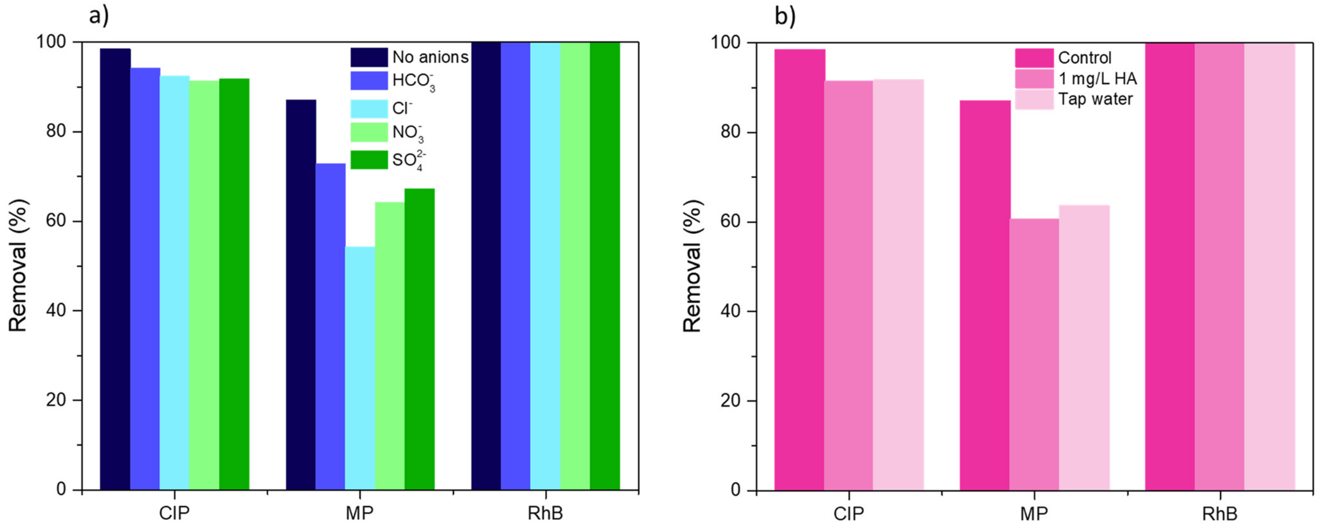

**Fig. 12** Effect of a) inorganic anions and b) humic acid (HA) and tap water on the degradation of CIP, MP, and RhB in the ternary-contaminant system under visible light irradiation for 40 min.

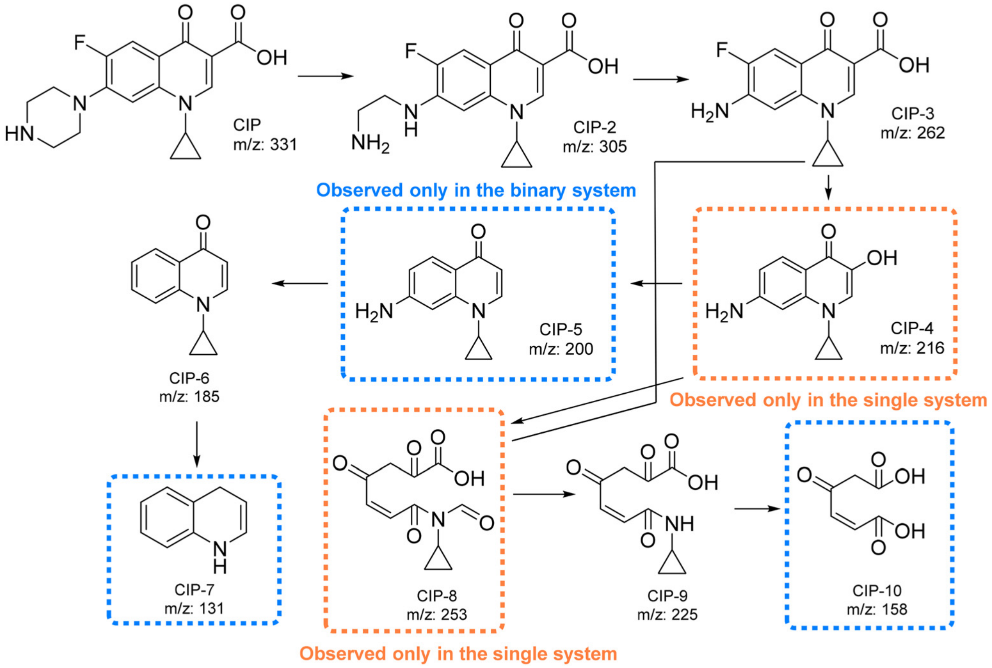

**Fig. 13** Proposed pathways for the degradation of CIP using $BiOCl_{0.9}I_{0.1}$ in the three different contaminant systems.

significant positive effect in the presence of other contaminants ($k$ = 0.2 $min^{-1}$ for a ternary-contaminant system *vs.* 0.08 and 0.02 $min^{-1}$ for single and binary-contaminant system, respectively) (Fig. S10a†). To get additional information, the CIP degradation pathways were examined by LC-MS analyses in the three contaminant systems (Fig. S15–S20†). As illustrated in Fig. 13, the presence of MP or MP/RhB in the studied water does not significantly alter the degradation pathway. Nevertheless, it should be noted that although there is a clear consistency between the results obtained in the three contaminant systems, some molecules of the proposed pathways only appear in some of the studied mixtures of contaminants.

First, the piperazine moiety seems to undergo oxidation, resulting in the formation of CIP-2 ($m/z$ = 305) (Fig. S16, S18 and S20†).[54] Subsequently, the $C_2H_5N$ group is lost, generating CIP-3 ($m/z$ = 262)[55] (Fig. S16, S18 and S20†), which then suffers a decarboxylation to form CIP-4 ($m/z$ = 216). This molecule (CIP-4) is only observed in the single system (Fig. S16†). On the other hand, in the binary system (CIP/MP), the CIP degradation also generates CIP-5 ($m/z$ = 200) through a defluorination reaction (Fig. S18†). Subsequently, the amino moiety seems to be eliminated, leading to the formation of CIP-6 ($m/z$ = 185) (Fig. S16, S18, and S20†). Finally, CIP-7 ($m/z$ = 131) is presumably formed through the cleavage of the cyclopropyl and the loss of the ketone moiety (observed only in the binary system) (Fig. S19†). Additionally, the opening of the quinolone and benzene rings of CIP-3 (ref. 56) or CIP-4 (ref. 57) results in the formation of CIP-8 (observed only in the single system), which undergoes further degradations to generate CIP-9 (Fig. S16, S18, and S20†) and CIP-10 (observed only in the binary system) (Fig. S18†).

In addition, assessing the toxicity of CIP and its degradation products is essential for measuring the effectiveness of contaminant degradation. The Estimation Software Tool (T.E.S.T.), developed by the United States Environmental Protection Agency, was used to conduct the study (Table S3†), which is focused in predicting the $IC_{50}$ for fish and *Daphnia magna*. For fish, only CIP-3 presents slightly higher toxicity than CIP, and its presence in the mass spectra is observed only during the early time measurement, indicating that its degradation is highly likely and its presence in the water is temporary. For *Daphnia magna*, most of the molecules generated show lower toxicity than for fish, being CIP-5 and CIP-6 those that show the highest toxicity (8.38 and 4.17 mg $L^{-1}$ respectively). As the degradation process progresses, the toxicity of the organic moieties present in the water diminishes, with particular attention to the final molecules in the degradation pathway. These molecules are categorized solely as either harmful for fish or non-harmful for *Daphnia magna*. Consequently, it can be concluded that significant detoxification of CIP from the tested mixtures has been successfully accomplished.

Finally, the stability of the optimal $BiOCl_{0.9}I_{0.1}$ photocatalyst was examined through recycling experiments, in single and mixed CIP/MP/RhB systems. The photocatalyst was able to maintain its initial photodegradation activity for up to 4 cycles during MP degradation (Fig. S21†). The remaining material was analyzed by XRD (Fig. S22†), and the pattern obtained after 4 cycles revealed minimal to no difference compared to the fresh material, indicating that $BiOCl_{0.9}I_{0.1}$ is a stable photocatalyst. In the mixed system (Fig. S23†), the photocatalyst also preserved its efficiency in removing RhB after 4 cycles showing a degradation of more than 60% of CIP and MP. The XRD analysis of $BiOCl_{0.9}I_{0.1}$ after 4 cycles (Fig. S24†) verified the robustness of the photocatalyst, as its structure seems to remain unaltered.

## 4. Conclusions

In this work the chloride or bromide anions of BiOCl or BiOBr, have been replaced by iodine anions, resulting in the formation of bismuth oxyhalide solid solutions, namely, $BiOCl_{0.9}I_{0.1}$ and $BiOBr_{0.9}I_{0.1}$, respectively. The incorporation of iodine significantly enhanced the photocatalytic activity under visible light irradiation compared to BiOCl and BiOBr materials, with MP degradation rates of 91.1% and 85.4% for $BiOCl_{0.9}I_{0.1}$ and $BiOBr_{0.9}I_{0.1}$ *vs.* 2% and 15% for BiOCl and BiOBr, respectively. Both solid solutions demonstrated a higher efficiency in the degradation and removal of a mixture of contaminants (including CIP, MP and RhB) compared to eliminating polluted water samples with a single contaminant. Remarkably, $BiOCl_{0.9}I_{0.1}$ demonstrated the highest photodegradation activity in mixtures of coexisting contaminants, completely removing RhB and CIP in 10 and 40 min, respectively, and degrading more than 85% of MP within 40 min.

The results revealed that the presence of RhB accelerates the degradation of both MP and CIP contaminants due to the enhanced generation of superoxide radicals through a RhB-sensitization mechanism. The excellent removal efficiency of CIP and RhB by $BiOCl_{0.9}I_{0.1}$ was maintained in different matrix waters (*i.e.* waters with the presence of inorganic species, organic matter and tap water). The superior performance of $BiOCl_{0.9}I_{0.1}$ is attributed to its effective charge transfer to the contaminants, low recombination of photogenerated charges, and enhanced photocurrent response, as confirmed by the complete series of optical and electrochemical experiments carried out in this work. Thus, this study paves the way for the effective application of visible-light-activated bismuth photocatalysis for the simultaneous elimination of multiple pollutants from wastewater.

## Data availability

The data supporting this article have been included as part of the ESI.†

## Conflicts of interest

The authors declare that they have no known competing financial interests or personal relationships that could have appeared to influence the work reported in this paper.

## Acknowledgements

We would like to thank funding from the research project PID2022-136417NB-I00 financed by MCIU/AEI/10.13039/501100011033/ and "ERDF A way of making Europe". We would also like to thank the support of Universidad Rey Juan Carlos to our research group COMET-NANO through the project M3271.

## References

1 K. Y. Pete, J. Kabuba, B. Otieno and A. Ochieng, Modeling adsorption and photocatalytic treatment of recalcitrant contaminant on multi-walled carbon/$TiO_2$ nanocomposite, *Environ. Sci. Pollut. Res.*, 2023, **30**, 94154–94165.

2 C. Mutuku, Z. Gazdag and S. Melegh, Occurrence of antibiotics and bacterial resistance genes in wastewater: resistance mechanisms and antimicrobial resistance control approaches, *World J. Microbiol. Biotechnol.*, 2022, **38**, 152.

3 Y. Yang, X. Zhang, J. Jiang, J. Han, W. Li, X. Li, K. M. Yee Leung, S. A. Snyder and P. J. J. Alvarez, Which Micropollutants in Water Environments Deserve More Attention Globally?, *Environ. Sci. Technol.*, 2022, **56**, 13–29.

4 D. Błędzka, J. Gromadzińska and W. Wąsowicz, Parabens. From environmental studies to human health, *Environ. Int.*, 2014, **67**, 27–42.

5 C. Maia, C. A. Sousa, H. Sousa, F. Vale and M. Simões, Parabens removal from wastewaters by microalgae – Ecotoxicity, metabolism and pathways, *Chem. Eng. J.*, 2023, **453**, 139631.

6 M. Ren, H. Liu, J. Qu, Y. Zhang, Y. Ma and X. Yuan, The different paths and potential risks of photo(−electro)-catalytic degradation for rhodamine B in water by graphene/$TiO_2$ membrane, *Environ. Sci. Pollut. Res.*, 2018, **25**, 13988–13999.

7 J. J. Urban, Emerging Scientific and Engineering Opportunities within the Water-Energy Nexus, *Joule*, 2017, **1**, 665–688.

8 E. P. Costa, M. C. V. M. Starling and C. C. Amorim, Simultaneous removal of emerging contaminants and disinfection for municipal wastewater treatment plant effluent quality improvement: a systemic analysis of the literature, *Environ. Sci. Pollut. Res.*, 2021, **28**, 24092–24111.

9 M. Xu, J. Yang, C. Sun, L. Liu, Y. Cui and B. Liang, Performance enhancement strategies of bi-based photocatalysts: A review on recent progress, *Chem. Eng. J.*, 2020, **389**, 124402.

10 X. Zhang, C. Wang, L. Wang, G. Huang, W. Wang and H. Yu, Fabrication of BiOBrxI1−x photocatalysts with tunable visible light catalytic activity by modulating band structures, *Sci. Rep.*, 2016, **6**, 22800.

11 L. Kong, J. Guo, J. W. Makepeace, T. Xiao, H. F. Greer, W. Zhou, Z. Jiang and P. P. Edwards, Rapid synthesis of $BiOBr_xI_{1-x}$ photocatalysts: Insights to the visible-light photocatalytic activity and strong deviation from Vegard's law, *Catal. Today*, 2019, **335**, 477–484.

12 Q. Y. Liu, G. Han, Y. F. Zheng and X. C. Song, Synthesis of $BiOBr_xI_{1-x}$ solid solutions with dominant exposed {0 0 1} and {1 1 0} facets and their visible-light-induced photocatalytic properties, *Sep. Purif. Technol.*, 2018, **203**, 75–83.

13 J. Xie, Y. Cao, D. Jia and Y. Li, Dahlia-shaped $BiOCl_xI_{1-x}$ structures prepared by a facile solid-state method: Evidence and mechanism of improved photocatalytic degradation of rhodamine B dye, *J. Colloid Interface Sci.*, 2017, **503**, 115–123.

14 L. Liang, J. Wang, R. Wu, Z. Li, X. Yan and Y. Lv, Preparation of $BiOCl_{1-x}I_x$ solid solution and its visible light photocatalytic performance, *J. Mater. Sci.: Mater. Electron.*, 2020, **31**, 2817–2825.

15 R. Lu, A. H. Zahid and Q. Han, Insight into the photocatalytic mechanism of the optimal x value in the $BiOBr_xI_{1-x}$, $BiOCl_xI_{1-x}$ and $BiOCl_xBr_{1-x}$ series varying with pollutant type, *Nanoscale*, 2022, **14**, 13711–13721.

16 F. J. Lopez, E. Pitarch, A. M. Botero-Coy, D. Fabregat-Safont, M. Ibáñez, J. M. Marin, A. Peruga, N. Ontañón, S. Martínez-Morcillo, A. Olalla, Y. Valcárcel, I. Varó and F. Hernández, Removal efficiency for emerging contaminants in a WWTP from Madrid (Spain) after secondary and tertiary treatment and environmental impact on the Manzanares River, *Sci. Total Environ.*, 2022, **812**, 152567.

17 N. Adimalla and H. Qian, Geospatial Distribution and Potential Noncarcinogenic Health Risk Assessment of Nitrate Contaminated Groundwater in Southern India: A Case Study, *Arch. Environ. Contam. Toxicol.*, 2021, **80**, 107–119.

18 L. Han, B. Li, H. Wen, Y. Guo and Z. Lin, Photocatalytic degradation of mixed pollutants in aqueous wastewater using mesoporous 2D/2D $TiO_2$(B)-BiOBr heterojunction, *J. Mater. Sci. Technol.*, 2021, **70**, 176–184.

19 A. A. Meshram and S. M. Sontakke, Rapid degradation of metamitron and highly complex mixture of pollutants using MIL-53(Al) integrated combustion synthesized TiO2, *Adv. Powder Technol.*, 2021, **32**, 3125–3135.

20 G. Zhang, L. Cai, Y. Zhang and Y. Wei, $Bi^{5+}$, $Bi^{(3-x)+}$, and Oxygen Vacancy Induced BiOClxI1−x Solid Solution toward Promoting Visible-Light Driven Photocatalytic Activity, *Chem. – Eur. J.*, 2018, **24**, 7434–7444.

21 X. Zhang, C. Wang, L. Wang, G. Huang, W. Wang and H. Yu, Fabrication of BiOBrxI1−x photocatalysts with tunable visible light catalytic activity by modulating band structures, *Sci. Rep.*, 2016, **6**, 22800.

22 K. Xu, D. Xu, Z. Li, S. Zhang, L. Tong, J. Peng, S. Zhang, J. Shen and X. Chen, Enhanced visible-light photocatalytic degradation of ciprofloxacin hydrochloride by bulk iodine doped BiOCl with rich oxygen vacancy, *Appl. Surf. Sci.*, 2022, **578**, 152083.

23 S. S. Imam, R. Adnan and N. H. Mohd Kaus, Room-temperature in situ synthesis of BiOBr/$Bi_2O_3$ composites for the catalytic degradation of ciprofloxacin using indoor fluorescent light illumination, *SN Appl. Sci.*, 2019, **1**, 845.

24 Y. Yan, Z. Zhou, Y. Cheng, L. Qiu, C. Gao and J. Zhou, Template-free fabrication of α- and β-$Bi_2O_3$ hollow spheres and their visible light photocatalytic activity for water purification, *J. Alloys Compd.*, 2014, **605**, 102–108.

25 W. Tang, Y. Zhang, H. Guo and Y. Liu, Heterogeneous activation of peroxymonosulfate for bisphenol AF degradation with $BiOI_{0.5}Cl_{0.5}$, *RSC Adv.*, 2019, **9**, 14060–14071.

26 V. Vivier, C. Cachet-Vivier, S. Mezaille, B. L. Wu, C. S. Cha, J. Nedelec, M. Fedoroff, D. Michel and L. T. Yu, Electrochemical Study of $Bi_2O_3$ and $Bi_2O_2CO_3$ by Means of a Cavity Microelectrode. I. Observed Phenomena and Direct Analysis of Results, *J. Electrochem. Soc.*, 2000, **147**, 4252.

27 V. Vivier, A. Régis, G. Sagon, J. Nedelec, L. T. Yu and C. Cachet-Vivier, Cyclic voltammetry study of bismuth oxide $Bi_2O_3$ powder by means of a cavity microelectrode coupled with Raman microspectrometry, *Electrochim. Acta*, 2001, **46**, 907–914.

28 J. Ortiz-Bustos, M. Fajardo, I. del Hierro and Y. Pérez, Versatile titanium dioxide nanoparticles prepared by surface-grown polymerization of polyethylenimine for photodegradation and catalytic CC bond forming reactions, *Mol. Catal.*, 2019, **475**, 110501.

29 Z. Cui, H. Song, S. Ge, W. He and Y. Liu, Fabrication of BiOCl/BiOBr hybrid nanosheets with enhanced superoxide radical dominating visible light driven photocatalytic activity, *Appl. Surf. Sci.*, 2019, **467–468**, 505–513.

30 A. Kumar, G. Shalini, M. Sharma, A. Naushad, S. Kumar, C. G. Kalia and G. T. Mola, Facile hetero-assembly of superparamagnetic $Fe_3O_4$/$BiVO_4$ stacked on biochar for solar photo-degradation of methyl paraben and pesticide removal from soil, *J. Photochem. Photobiol., A*, 2017, **337**, 118–131.

31 X. Su and D. Wu, Facile construction of the phase junction of BiOBr and Bi4O5Br2 nanoplates for ciprofloxacin photodegradation, *Mater. Sci. Semicond. Process.*, 2018, **80**, 123–130.

32 N. Y. Tashkandi, S. M. Albukhari and A. A. Ismail, Mesoporous $BiVO_4$/$TiO_2$ heterojunction: enhanced photoabsorption and photocatalytic ability through promoted charge transfer, *Environ. Sci. Pollut. Res.*, 2022, **29**, 78472–78482.

33 T. Qin, J. Wei, C. Zhou, X. Zeng, J. Zhou and Y. Li, Directional crystal facets deposition constructed $BiVO_4$/Ag/$MnO_2$ with plasmon resonance for enhanced photocatalytic degradation of antibiotics in water, *Sep. Purif. Technol.*, 2023, **317**, 123793.

34 M. Z. Abid, A. Ilyas, K. Rafiq, A. Rauf, M. A. Nadeem, A. Waseem and E. Hussain, Simultaneous elimination of toxic dyes, ciprofloxacin and Cr(vi) contents from polluted water: escalating surface plasmon electrons of Ag cocatalysts on $BiVO_4$ microstructures, *Environ. Sci.: Water Res. Technol.*, 2023, **9**, 2238–2252.

35 X. Xiao, M. Lu, J. Nan, X. Zuo, W. Zhang, S. Liu and S. Wang, Rapid microwave synthesis of I-doped $Bi_4O_5Br_2$ with significantly enhanced visible-light photocatalysis for degradation of multiple parabens, *Appl. Catal., B*, 2017, **218**, 398–408.

36 Y. Cong, Y. Ji, Y. Ge, H. Jin, Y. Zhang and Q. Wang, Fabrication of 3D $Bi_2O_3$-BiOI heterojunction by a simple dipping method: Highly enhanced visible-light photoelectrocatalytic activity, *Chem. Eng. J.*, 2017, **307**, 572–582.

37 L. N. Thi, H. Tran Huu, T. N. Ngoc, N. S. M. Viswanath, H. T. T. Le, T. T. T. Phan, L. T. Nguyen, Q. T. H. Ta, H. Le Han, L. N. Tan and V. Vo, $BiOCl_{1-x}Br_x$ solid solution – Novel synthesis, highly-efficient visible-light-driven photocatalyst, and DFT study, *J. Alloys Compd.*, 2023, **960**, 170503.

38 H. Qin, J. Sun, D. Xia, H. Xu, Q. Yu, Y. Zheng and Y. Shi, Boosting nonradical process in BiOI/BiOCl heterostructure by interface oxygen vacancies, *Chem. Eng. J.*, 2022, **435**, 134847.

39 W. Li, Z. Liu, Y. Dong, L. Wang, Z. Liu, L. Zhang and Z. Qiao, Micellar interface modulation self-assembly strategy towards mesoporous bismuth oxychloride-based materials for boosting photocatalytic pharmaceuticals degradation, *Chem. Eng. J.*, 2022, **450**, 137897.

40 Y. Cherifi, A. Barras, A. Addad, B. Ouddane, P. Roussel, A. Chaouchi, S. Szunerits and R. Boukherroub, Simultaneous photocatalytic Cr(VI) reduction and phenol degradation over copper sulphide-reduced graphene oxide nanocomposite under visible light irradiation: Performance and reaction mechanism, *Chemosphere*, 2021, **268**, 128798.

41 L. Han, B. Li, H. Wen, Y. Guo and Z. Lin, Photocatalytic degradation of mixed pollutants in aqueous wastewater using mesoporous 2D/2D $TiO_2$(B)-BiOBr heterojunction, *J. Mater. Sci. Technol.*, 2021, **70**, 176–184.

42 V. Nguyen, L. Phan Thi, P. S. Chandana, H. Do, T. Pham, T. Lee, T. D. Nguyen, C. Le Phuoc and P. T. Huong, The degradation of paraben preservatives: Recent progress and sustainable approaches toward photocatalysis, *Chemosphere*, 2021, **276**, 130163.

43 X. Jia, J. Cao, H. Lin, M. Zhang, X. Guo and S. Chen, Transforming type-I to type-II heterostructure photocatalyst via energy band engineering: A case study of I-BiOCl/I-BiOBr, *Appl. Catal., B*, 2017, **204**, 505–514.

44 M. A. Oliva, J. Ortiz-Bustos, M. Cruz-Yusta, F. Martin, I. del Hierro, Y. Pérez, I. Pavlovic and L. Sánchez, 2D/2D NiTi-LDH/BiOBr photocatalyst with extraordinary NOx removal under visible light, *Chem. Eng. J.*, 2023, **470**, 144088.

45 H. Qin, J. Sun, D. Xia, H. Xu, Q. Yu, Y. Zheng and Y. Shi, Boosting nonradical process in BiOI/BiOCl heterostructure by interface oxygen vacancies, *Chem. Eng. J.*, 2022, **435**, 134847.

46 X. Zheng, W. Chen, M. Xu, C. Cai and F. Yang, Photocatalytic properties of BiOBr/BiOCl/AgBr ternary photocatalysts for degradation of RhB dye, *J. Nanopart. Res.*, 2023, **25**, 96.

47 Z. Ran, X. Wang, Y. Li, D. Yang, X. Zhao, K. Biswas, D. J. Singh and L. Zhang, Bismuth and antimony-based oxyhalides and chalcohalides as potential optoelectronic materials, *npj Comput. Mater.*, 2018, **4**, 14.

48 M. Tayebi, A. Tayyebi and B. Lee, Improved photoelectrochemical performance of molybdenum (Mo)-doped monoclinic bismuth vanadate with increasing donor concentration, *Catal. Today*, 2019, **328**, 35–42.

49 N. T. T. Hai, V. V. Tu, P. H. Long, D. T. Hien, N. T. T. Huong, P. H. Quynh, N. T. T. Phuong, N. M. Viet and P. Q. Thang, Improvement of Photocatalytic Degradation and Adsorption of Ciprofloxacin by Bismuth Oxyiodide, *Chem. Eng. Technol.*, 2023, **46**, 2404–2411.

50 F. Guo, J. Chen, J. Zhao, Z. Chen, D. Xia, Z. Zhan and Q. Wang, Z-scheme heterojunction g-$C_3N_4$@PDA/BiOBr with biomimetic polydopamine as electron transfer mediators for enhanced visible-light driven degradation of sulfamethoxazole, *Chem. Eng. J.*, 2020, **386**, 124014.

51 B. H. Graimed, Z. H. Jabbar, M. M. Alsunbuli, S. H. Ammar and A. G. Taher, Decoration of 0D $Bi_3NbO_7$ nanoparticles onto 2D $BiOIO_3$ nanosheets as visible-light responsive S-scheme photocatalyst for photo-oxidation of antibiotics in wastewater, *Environ. Res.*, 2024, **243**, 117854.

52 J. Liu, X. Chang, Y. Cheng, Z. Guo and Q. Yan, Construction of novel Ag/AgI/$Bi_4Ti_3O_{12}$ plasmonic heterojunction: A study focusing on the performance and mechanism of photocatalytic removal of tetracycline, *Chemosphere*, 2024, **352**, 141306.

53 J. Yang, L. Wang, J. Yang, C. Li and S. Zhong, Magnetic biochar coupled with bismuth tungstate for multiple antibiotic removal from contaminated water: Characteristics, performance, and competitive adsorption synergistic photocatalysis mechanism, *J. Environ. Chem. Eng.*, 2024, **12**, 111768.

54 X. Hu, X. Hu, Q. Peng, L. Zhou, X. Tan, L. Jiang, C. Tang, H. Wang, S. Liu, Y. Wang and Z. Ning, Mechanisms underlying the photocatalytic degradation pathway of ciprofloxacin with heterogeneous $TiO_2$, *Chem. Eng. J.*, 2020, **380**, 122366.

55 M. Murugalakshmi, K. Govindan, M. Umadevi, C. B. Breslin and V. Muthuraj, Fabrication of a $Sm_2O_3/In_2S_3$ photocatalyst for boosting ciprofloxacin oxidation and the Cr(VI) reduction: process parameters and degradation mechanism, *Environ. Sci.: Water Res. Technol.*, 2023, **9**, 1385–1402.

56 X. Wen, C. Niu, L. Zhang, C. Liang, H. Guo and G. Zeng, Photocatalytic degradation of ciprofloxacin by a novel Z-scheme $CeO_2$–Ag/AgBr photocatalyst: Influencing factors, possible degradation pathways, and mechanism insight, *J. Catal.*, 2018, **358**, 141–154.

57 G. Fan, C. Cai, S. Yang, B. Du, J. Luo, Y. Chen, X. Lin, X. Li and Y. Wang, Sonophotocatalytic degradation of ciprofloxacin by $Bi_2MoO_6/FeVO_4$ heterojunction: Insights into performance, mechanism and pathway, *Sep. Purif. Technol.*, 2022, **303**, 122251.